

# Efficient and stable emission of warm-white light from lead-free halide double perovskites

Jiajun Luo<sup>1,11</sup>, Xiaoming Wang<sup>2,11</sup>, Shunran Li<sup>1,11</sup>, Jing Liu<sup>1,11</sup>, Yueming Guo<sup>3</sup>, Guangda Niu<sup>1</sup>, Li Yao<sup>1</sup>, Yuhao Fu<sup>4</sup>, Liang Gao<sup>1,5</sup>, Qingshun Dong<sup>6</sup>, Chunyi Zhao<sup>7</sup>, Meiyong Leng<sup>1</sup>, Fusheng Ma<sup>6</sup>, Wenxi Liang<sup>1</sup>, Liduo Wang<sup>6</sup>, Shengye Jin<sup>7</sup>, Junbo Han<sup>8</sup>, Lijun Zhang<sup>4</sup>, Joanne Etheridge<sup>3,9</sup>, Jianbo Wang<sup>10</sup>, Yanfa Yan<sup>2\*</sup>, Edward H. Sargent<sup>5</sup> & Jiang Tang<sup>1\*</sup>

**Lighting accounts for one-fifth of global electricity consumption<sup>1</sup>. Single materials with efficient and stable white-light emission are ideal for lighting applications, but photon emission covering the entire visible spectrum is difficult to achieve using a single material. Metal halide perovskites have outstanding emission properties<sup>2,3</sup>; however, the best-performing materials of this type contain lead and have unsatisfactory stability. Here we report a lead-free double perovskite that exhibits efficient and stable white-light emission via self-trapped excitons that originate from the Jahn–Teller distortion of the  $\text{AgCl}_6$  octahedron in the excited state. By alloying sodium cations into  $\text{Cs}_2\text{AgInCl}_6$ , we break the dark transition (the inversion-symmetry-induced parity-forbidden transition) by manipulating the parity of the wavefunction of the self-trapped exciton and reduce the electronic dimensionality of the semiconductor<sup>4</sup>. This leads to an increase in photoluminescence efficiency by three orders of magnitude compared to pure  $\text{Cs}_2\text{AgInCl}_6$ . The optimally alloyed  $\text{Cs}_2(\text{Ag}_{0.60}\text{Na}_{0.40})\text{InCl}_6$  with 0.04 per cent bismuth doping emits warm-white light with  $86 \pm 5$  per cent quantum efficiency and works for over 1,000 hours. We anticipate that these results will stimulate research on single-emitter-based white-light-emitting phosphors and diodes for next-generation lighting and display technologies.**

Metal halide perovskites have rapidly advanced the field of optoelectronic devices because of their exceptional defect tolerance, low-cost solution processing and tunable emission across the visible spectrum<sup>5–8</sup>. For example, the photoluminescence quantum yield (PLQY) of perovskite nanocrystals is now close to unity<sup>9,10</sup>, and green and red electroluminescent devices have been reported to have external quantum efficiencies that reach 20.1%<sup>11–14</sup>. For lighting applications, white emission from a single emitter layer is of particular interest, because it simplifies device structure and avoids the self-absorption and colour instability seen in mixed and multiple emitters<sup>15</sup>.

Broadband and white emission typically originate from self-trapped excitons (STEs) that exist in semiconductors with localized carriers and a soft lattice<sup>16–18</sup>. Although hybrid metal halide perovskites, particularly those with low-dimensional crystal structures<sup>15,19–21</sup>, have received considerable attention as broadband-emission materials, they rarely achieve high PLQY<sup>21</sup>. Further challenges in their use as emitters include their reliance on water-soluble lead-based materials, unsatisfactory stability and a lack of systematic understanding of the origins of white emission.

Here we focused on the double perovskite  $\text{Cs}_2\text{AgInCl}_6$ , which is a promising material emitting warm-white light, in view of its broad spectrum (400–800 nm) and its all-inorganic and lead-free nature<sup>22–24</sup>.

We first performed first-principles density-functional-theory and many-body perturbation-theory calculations using the GW approximation and the Bethe–Salpeter equation (BSE) to understand the origins of the broadband emission in  $\text{Cs}_2\text{AgInCl}_6$ . The GW-BSE calculations indicated that the lowest exciton, which has a binding energy  $E_b$  of 0.25 eV, is dark (emits no photons) because the associated transition is parity-forbidden<sup>24</sup> (Fig. 1a). This exciton was calculated with the crystal structure fixed in its ground-state equilibrium, which represents the situation of the free exciton. We then investigated exciton–phonon coupling by relaxing the lattice, which represents the situation of the STEs (Fig. 1b). We found that the STEs in  $\text{Cs}_2\text{AgInCl}_6$  arise from a strong Jahn–Teller distortion of the  $\text{AgCl}_6$  octahedron (see inset of Fig. 1b); that is, the Ag–Cl bonds are elongated by 0.08 Å in the axial direction but compressed by 0.2 Å in the equatorial plane. Hole trapping at Ag atoms that changes the electronic configuration of Ag to  $4d^9$  favours a Jahn–Teller distortion. The STE has the same orbital character as the free exciton, indicating a parity-forbidden transition. The self-trapping energy  $E_{st}$  and lattice-deformation energy  $E_d$ —which are the excited-state and ground-state energy differences between the STE and free-exciton configurations, as shown in the configuration coordinate diagram of Fig. 1c—were calculated to be 0.53 eV and 0.67 eV, respectively. The emission energy was thus calculated to be  $E_{PL} = E_g - E_{st} - E_d - E_b = 1.82$  eV, where  $E_g = 3.27$  eV is the fundamental band-gap energy, based on GW calculations and experimental results. This value agrees with the experimental photoluminescence peak value<sup>22</sup> of 2 eV. The phonon frequency,  $\hbar\Omega_g$  ( $\hbar$ , reduced Planck constant), of the ground state, obtained by fitting the configuration coordinate diagram, is 18.3 meV, which agrees well with the phonon eigenmode of 17 meV. The corresponding eigenvector shows displacement in agreement with the Jahn–Teller distortion (Extended Data Fig. 1), consistent with the view that the Jahn–Teller distortion is responsible for STE formation in  $\text{Cs}_2\text{AgInCl}_6$ . Strong electron–phonon coupling, which is necessary for STE formation, is confirmed by the large Huang–Rhys<sup>25</sup> factor  $S = E_d/\hbar\Omega_g = 37$ , consistent with experimental results (Extended Data Fig. 2). With the phonon frequency  $\hbar\Omega_e = 17.4$  meV of the excited state, we can estimate the exciton self-trapping time as  $\tau = 2\pi/\Omega_e = 238$  fs, which indicates an ultrafast transition from a free exciton to an STE following photoexcitation. The calculated photoluminescence spectrum and a comparison with the experimental data are shown in Fig. 1d. Overall the agreement is good, except for the small deviations at 400–450 nm, which could be attributed to the free-exciton emission not accounted for in our calculations.

The above theoretical analysis indicates an extremely low PLQY for pure  $\text{Cs}_2\text{AgInCl}_6$ . The PLQY is defined as the ratio of the radiative

<sup>1</sup>Sargent Joint Research Center, Wuhan National Laboratory for Optoelectronics (WNLO) and School of Optical and Electronic Information, Huazhong University of Science and Technology (HUST), Wuhan, China. <sup>2</sup>Department of Physics and Astronomy and Wright Center for Photovoltaics Innovation and Commercialization, The University of Toledo, Toledo, OH, USA. <sup>3</sup>Department of Materials Science and Engineering, Monash University, Clayton, Victoria, Australia. <sup>4</sup>State Key Laboratory of Superhard Materials, Key Laboratory of Automobile Materials of MOE, and School of Materials Science and Engineering, Jilin University, Changchun, China. <sup>5</sup>Department of Electrical and Computer Engineering, University of Toronto, Toronto, Ontario, Canada. <sup>6</sup>Key Laboratory of Organic Optoelectronics and Molecular Engineering of Ministry of Education, Department of Chemistry, Tsinghua University, Beijing, China. <sup>7</sup>State Key Laboratory of Molecular Reaction Dynamics and Collaborative Innovation Center of Chemistry for Energy Materials (iChEM), Dalian Institute of Chemical Physics, Chinese Academy of Sciences, Dalian, China. <sup>8</sup>Wuhan National High Magnetic Field Center, Huazhong University of Science and Technology (HUST), Wuhan, China. <sup>9</sup>Monash Centre for Electron Microscopy, Monash University, Clayton, Victoria, Australia. <sup>10</sup>School of Physics and Technology, Center for Electron Microscopy, MOE Key Laboratory of Artificial Micro- and Nano-structures, and Institute for Advanced Studies, Wuhan University, Wuhan, China. <sup>11</sup>These authors contributed equally: Jiajun Luo, Xiaoming Wang, Shunran Li, Jing Liu. \*e-mail: yanfa.yan@utoledo.edu; jtang@mail.hust.edu.cn

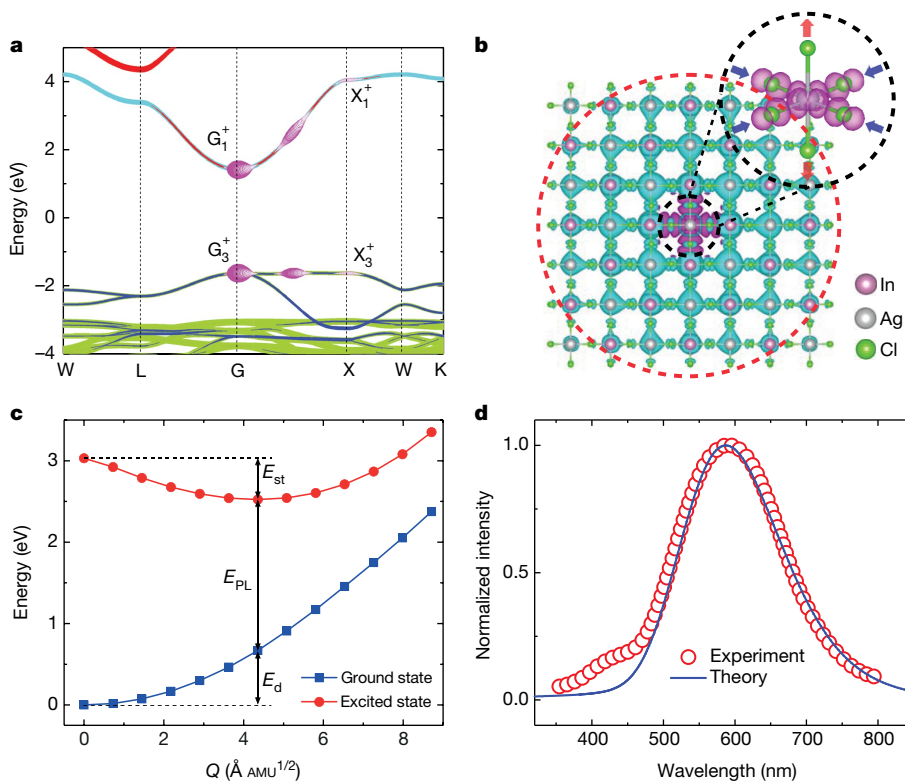


**Fig. 1 | Computational studies of the STEs in  $\text{Cs}_2\text{AgInCl}_6$ .** **a**, GW band structure of  $\text{Cs}_2\text{AgInCl}_6$ . The orbital characters and free-exciton wavefunction are plotted as a fat-band structure. The green, blue, cyan and red colours denote the Cl 3p, Ag 4d, In 5s and Ag 5s orbitals, respectively. The magenta circles indicate the lowest free-exciton amplitude  $|A_{vc\mathbf{k}}|$ , where  $|S\rangle = \sum_{vc\mathbf{k}} A_{vc\mathbf{k}} |vc\rangle$  is the exciton wavefunction,  $v$  and  $c$  denote the valence and conduction states, and  $\mathbf{k}$  is the wavevector.  $|S\rangle$  is derived from the electron and hole states with the same parity (labels at the zone centre G and X) along GX, implying a dark transition. **b**, STE in  $\text{Cs}_2\text{AgInCl}_6$ . Cs atoms are omitted for clarity. The cyan and magenta isosurfaces represent the electron and hole orbital densities ( $\rho = \langle \psi | \psi \rangle$ ), respectively. The

recombination rate ( $k_{\text{rad}}$ ) to the sum of the radiative and non-radiative ( $k_{\text{non}}$ ) recombination rates. From Fermi's golden rule,  $k_{\text{rad}}$  is proportional to the transition dipole moment,  $\mu = \langle \varphi_{\text{h}} | \hat{\mu} | \varphi_{\text{e}} \rangle$ , where  $\varphi_{\text{e}}$  and  $\varphi_{\text{h}}$  are the electron and hole wavefunctions, respectively, and  $\hat{\mu}$  is the electric dipole operator. The dark transition of the free excitons and STEs in  $\text{Cs}_2\text{AgInCl}_6$  results in extremely low radiative recombination rates, leading to low PLQY ( $<0.1\%$ ; Extended Data Fig. 2d). Increasing  $k_{\text{rad}}$  and reducing  $k_{\text{non}}$  are two strategies to enhance the PLQY. The first and most critical step towards improving the PLQY is to break the parity-forbidden transition by manipulating the symmetry of the STE wavefunction. A practical approach to this end is to partially substitute Ag with an element that can sustain the double-perovskite structure, but has a distinctively different electronic configuration to Ag, such as a group-IA element (alkali metal). We therefore explored alloying Na into  $\text{Cs}_2\text{AgInCl}_6$ . Broadband emission was also observed in pure  $\text{Cs}_2\text{NaInCl}_6$  (Extended Data Fig. 3), but with very low efficiency due to strong phonon emission, as indicated by a simulated high Huang–Rhys factor of 80 at the excited state. We note that the Huang–Rhys factor can potentially serve as the figure of merit for the design of efficient white-light-emitting materials from STEs (Extended Data Table 1). Because the lattice mismatch between  $\text{Cs}_2\text{NaInCl}_6$  and  $\text{Cs}_2\text{AgInCl}_6$  is as low as 0.30% (Supplementary Table 1), we anticipated that  $\text{Na}^+$  could be incorporated uniformly into  $\text{Cs}_2\text{AgInCl}_6$ , without causing detrimental defects or phase separation. For the synthesis, CsCl, NaCl, AgCl and  $\text{InCl}_3$  precursors were mixed into an HCl solution in a hydrothermal autoclave, which was heated for a given time and then slowly cooled down, resulting in white precipitates as final products. This straightforward synthesis gave a product yield of nearly 90%.

electron state (red dashed circle) is rather extended and the hole state (black dashed circle) is compact, consistent with the small (large) effective mass of the conduction (valence) band shown in **a**. The inset shows the Jahn–Teller distortion of the  $\text{AgCl}_6$  octahedron. Here the hole isosurface is obvious, whereas the electron isosurface is invisible owing to its small density. **c**, Configuration coordinate diagram for the STE formation.  $E_{\text{st}}$ ,  $E_{\text{d}}$  and  $E_{\text{PL}}$  are the self-trapping, lattice-deformation and emission energies, respectively. **d**, Calculated photoluminescence spectrum compared with the experimental result. The calculated curve has been shifted to align its maximum with that of the experimentally measured curve for better comparison.

X-ray diffraction (XRD) patterns of a series of compositions (Fig. 2a) confirmed the pure double-perovskite phase. The intensity of the (111) diffraction peak (marked with an asterisk in Fig. 2a) is related to the Na/Ag composition through the dispersion factor of the Na, Ag and In atoms<sup>26</sup>. These agree well with the compositions determined using inductively coupled plasma optical emission spectrometry (ICP-OES; Supplementary Table 3). This observation also suggests a high degree of B(I) and B'(III) site ordering and negligible antisite defects (Supplementary Fig. 2). The refined lattice parameters follow a linear increase upon Na substitution, indicating solid-solution behaviour with  $\text{Na}^+/\text{Ag}^+$  randomly distributed<sup>27</sup> at B(I) sites in  $\text{Cs}_2\text{Ag}_x\text{Na}_{1-x}\text{InCl}_6$  (Extended Data Fig. 4). Upon Na alloying, an evident excitonic absorption peak emerged near 365 nm, and the intensity of white emission was enhanced by three orders of magnitude compared to the pure  $\text{Cs}_2\text{AgInCl}_6$  and  $\text{Cs}_2\text{NaInCl}_6$  (Fig. 2b). A similar phenomenon was also found in Li-doped  $\text{Cs}_2\text{AgInCl}_6$  and Na-doped  $\text{Cs}_2\text{AgSbCl}_6$  (Extended Data Fig. 5), suggesting a general trend of alkali-metal-induced photoluminescence enhancement in double perovskites. We then recorded the photoluminescence spectra of a series of  $\text{Cs}_2\text{Ag}_x\text{Na}_{1-x}\text{InCl}_6$  powders by varying the measurement temperatures, and found that the extracted activation energy (Supplementary Figs. 6, 7) increases monotonically with increasing Na content, suggesting suppression of the non-radiative process and thermal quenching upon Na alloying. With optimized Na content, Bi doping and slow cooling, we obtained the highest PLQY of  $(86 \pm 5)\%$  at a Na content of about 40% (Fig. 2c, Supplementary Fig. 8). To the best of our knowledge, this PLQY represents the highest efficiency reported for white-emitting materials (Supplementary Table 4). The best-

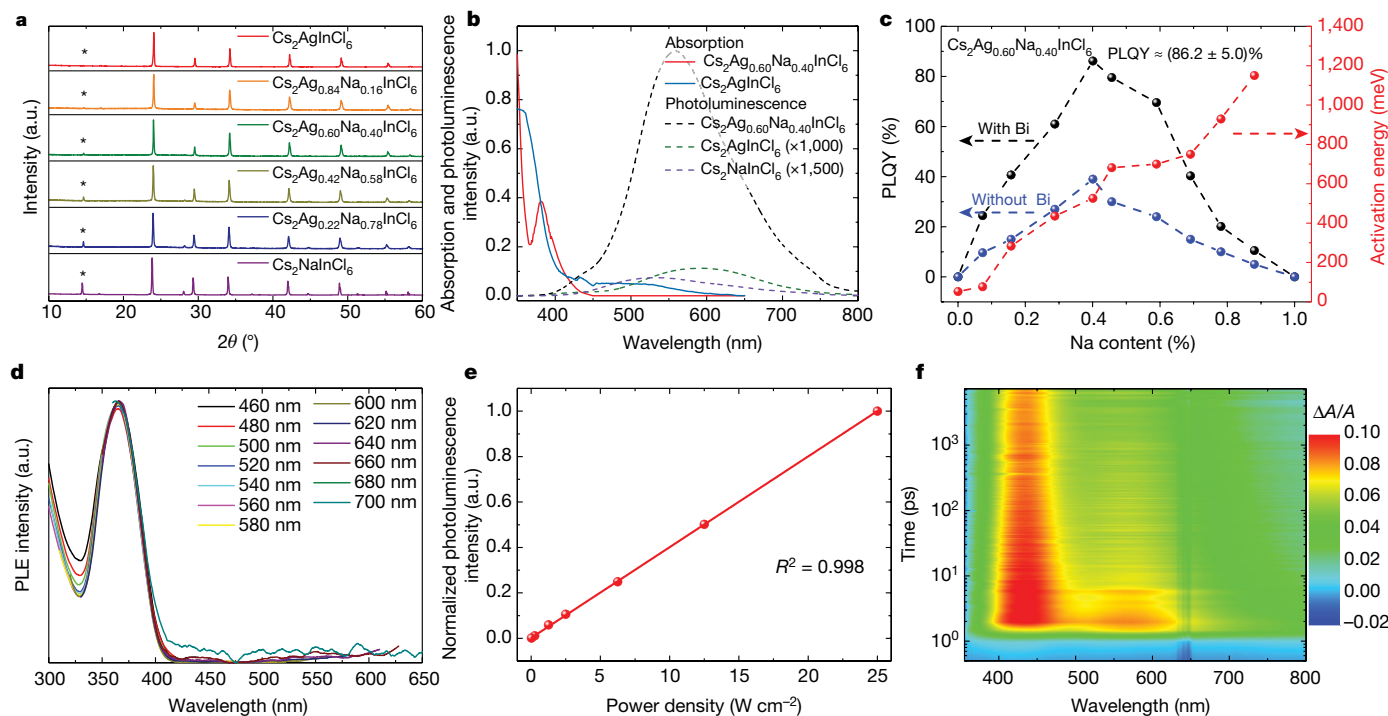


**Fig. 2 | Characterization of  $\text{Cs}_2\text{Ag}_x\text{Na}_{1-x}\text{InCl}_6$  with different Na content.** All samples were doped using a small amount (0.04%, atomic ratio to In) of Bi, and the compositions were determined from ICP-OES results (Supplementary Table 3). **a**, XRD patterns of  $\text{Cs}_2\text{Ag}_x\text{Na}_{1-x}\text{InCl}_6$  powders with different Na content. The asterisk marks the (111) diffraction peak.  $\theta$ , diffraction angle; a.u., arbitrary units. **b**, Optical absorption (solid lines) and photoluminescence (dashed lines) spectra of pure  $\text{Cs}_2\text{AgInCl}_6$  and  $\text{Cs}_2\text{Ag}_{0.60}\text{Na}_{0.40}\text{InCl}_6$ . **c**, Activation energy and PLQY of  $\text{Cs}_2\text{Ag}_x\text{Na}_{1-x}\text{InCl}_6$  powder versus Na content. The reproducibility of the PLQY results is shown in Supplementary Fig. 8d (best, about 86.2%;

performing white-light-emitting lead halide perovskites  $\text{C}_4\text{N}_2\text{H}_{14}\text{PbBr}_4^{28}$  and  $\text{CuGaS}_2/\text{ZnS}$  quantum dots<sup>29</sup> exhibit PLQYs of 20% and 73%, respectively. The  $\text{Bi}^{3+}$  incorporation is believed to improve crystal perfection and promote exciton localization<sup>30</sup>, further enhancing the PLQY (Extended Data Fig. 6).

The STE origin of the white emission was further experimentally confirmed via photoluminescence excitation (PLE) spectra (Fig. 2d). For emission from 460 to 700 nm, the PLE spectra exhibit identical shapes and features, indicating that the white emission originates from the relaxation of the same excited state. The experimental observations that the PLE spectra decrease to nearly zero at wavelengths above 400 nm, that the emission intensity from  $\text{Cs}_2\text{Ag}_{0.60}\text{Na}_{0.40}\text{InCl}_6$  exhibits a linear dependence on the excitation power (Fig. 2e) and that the PLQY results are independent from the photoexcitation power (Supplementary Fig. 9) all suggest that the emission does not arise from permanent defects. Surface-defect emission is also ruled out by the comparable photoluminescence intensity of single crystals and ball-milled powders (Supplementary Fig. 10). The transient absorption data further provide direct evidence of STEs<sup>17</sup>. With 325-nm-wavelength laser photoexcitation,  $\text{Cs}_2\text{Ag}_{0.60}\text{Na}_{0.40}\text{InCl}_6$  exhibited a broad photoinduced absorption at energies across the visible spectrum (Fig. 2f, Supplementary Fig. 11), with an onset time of about 500 fs, consistent with our calculated exciton self-trapping time.

We performed further theoretical analysis to understand the trend of the PLQY as a function of Na content. In Fig. 3a, we show the calculated transition dipole moment of  $\text{Cs}_2\text{Ag}_{1-x}\text{Na}_x\text{InCl}_6$  as a function of Na concentration. It is clear that with the increase of Na content, the transition dipole moment first increases and then decreases, reflecting the observed composition-dependent PLQY. Figure 3b compares the electron wavefunction of the STEs before and after the Na alloying. Na incorporation breaks the inversion symmetry of the  $\text{Cs}_2\text{AgInCl}_6$  lattice and changes the electron wavefunction at the Ag site from symmetric to

asymmetric; this results in a parity change in the STE wavefunction and consequently allows radiative recombination. Because  $\text{Na}^+$  contributes to neither the conduction-band minimum nor the valence-band maximum of the alloy, the second effect of Na incorporation is to reduce the electronic dimensionality<sup>4</sup> of the  $\text{Cs}_2\text{AgInCl}_6$  lattice by partially isolating the  $\text{AgCl}_6$  octahedra (Supplementary Fig. 12). The newly formed  $\text{NaCl}_6$  octahedra serve as barriers that confine the spatial distribution of the STEs (Fig. 3c), thus enhancing the electron and hole orbital overlap and increasing the transition dipole moment. For example, the radius of the STE is reduced from more than 20 Å for the pure  $\text{Cs}_2\text{AgInCl}_6$  to only 9 Å with 50% Na incorporation, which increases the transition dipole moment from zero to 0.07 (in arbitrary units, a.u.).

Two factors account for the decreased PLQY upon further increasing the Na content. For Na-rich compounds, the electron remains strongly confined within a single In octahedron (In 5s and Cl 3p), and the hole is always located on the Ag 4d orbital and the neighbouring Cl 3p orbitals (Fig. 3d). Therefore, the orbital spatial overlap between electrons and holes for the STEs, and hence the transition dipole moment, is markedly reduced. The second factor is the increased non-radiative loss in the Na-rich alloy. We found that the excited- and ground-state curves cross in the configuration coordinate diagram of pure  $\text{Cs}_2\text{NaInCl}_6$  (Fig. 3e), which means that some photoexcited electrons can recombine with holes non-radiatively through phonon emission. The resulting diminished transition dipole moment and enhanced non-radiative recombination rates explain the decreased PLQY for Na-rich alloys.

The photoluminescence spectrum of the best-performing  $\text{Cs}_2\text{Ag}_{0.60}\text{Na}_{0.40}\text{InCl}_6$  powder exhibits extended overlap with the sensitivity of the human eye to optical wavelengths (that is, the luminosity function) (Fig. 3a), which enables a theoretical luminous efficacy reaching about 373  $\text{lm W}^{-1}$ . Emission stability is another

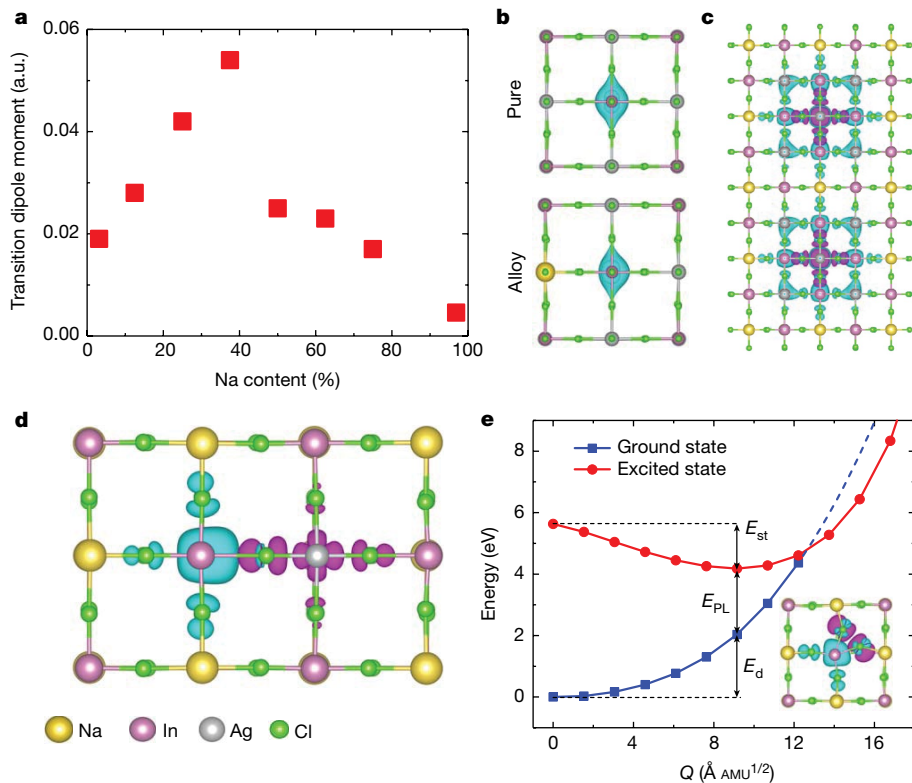


**Fig. 3 | Mechanistic investigations of PLQY in  $\text{Cs}_2\text{Ag}_{1-x}\text{Na}_x\text{InCl}_6$ .** **a**, Transition dipole moment,  $\mu$ , as a function of Na content in  $\text{Cs}_2\text{Ag}_{1-x}\text{Na}_x\text{InCl}_6$ . Assuming constant non-radiative recombination, the PLQY is proportional to  $\mu$ . **b**, Parity change of the electron wavefunction (isosurface at Ag site; see the key in the inset of **d**) of the STE before and after Na incorporation. **c**, Configuration showing the strengthened STE confinement by the surrounding  $\text{NaCl}_6$  octahedra. The STEs are confined within two lattice parameters surrounded by the  $\text{NaCl}_6$  octahedra. **d**, STE in Na-rich  $\text{Cs}_2\text{Ag}_{1-x}\text{Na}_x\text{InCl}_6$ . The STE is located in two neighbouring octahedra ( $\text{AgCl}_6$  and  $\text{InCl}_6$ ) with the hole derived from the Ag  $4d/\text{Cl}$   $3p$  orbitals and the electron from In  $5s/\text{Cl}$   $3p$  orbitals. **e**, Configuration coordinate diagram of the STE formation in  $\text{Cs}_2\text{NaInCl}_6$  (inset). The STE is located within a single distorted  $\text{InCl}_6$  octahedron. The hole is located at the well known  $V_k$  centre, that is, a  $\text{Cl}_2^-$  dimer ion, whereas the electron is derived from In  $5s/\text{Cl}$   $3p$  orbitals. The separation of the electron and hole makes the optical transition very weak. In **b–e**, the cyan and magenta isosurfaces denote electrons and holes, respectively.

key, yet very challenging, parameter for lighting applications. The  $\text{Cs}_2\text{Ag}_{0.60}\text{Na}_{0.40}\text{InCl}_6$  materials demonstrated little emission degradation when tested from 233 K to 343 K. A version of the material slightly richer in Na ( $\text{Na}/(\text{Ag} + \text{Na}) = 0.46$ ) showed stable emission up to 393 K (Supplementary Fig. 13). We further annealed our  $\text{Cs}_2\text{Ag}_{0.60}\text{Na}_{0.40}\text{InCl}_6$  powders on a hotplate at  $150^\circ\text{C}$  for 1,000 h and observed little photoluminescence decay of the white emission (Fig. 4b). We propose that the strongly bound excitons and nearly defect-free lattice of  $\text{Cs}_2\text{Ag}_{0.60}\text{Na}_{0.40}\text{InCl}_6$  prevent photoluminescence quenching and that

the all-inorganic composition also helps resist thermal stress (decomposition temperature of up to about 863 K; Supplementary Fig. 14).

We fabricated a white-emission light-emitting diode (LED) by directly pressing the  $\text{Cs}_2\text{Ag}_{0.60}\text{Na}_{0.40}\text{InCl}_6$  powders onto a commercial ultraviolet LED chip, without using epoxy or silica encapsulation for protection. With the contribution from the blue light of the ultraviolet LED chip (380–410 nm), the device has CIE coordinates (0.396, 0.448), located at a warm-white point with a correlated colour temperature of 4,054 K, which fulfils the requirements for indoor lighting. The

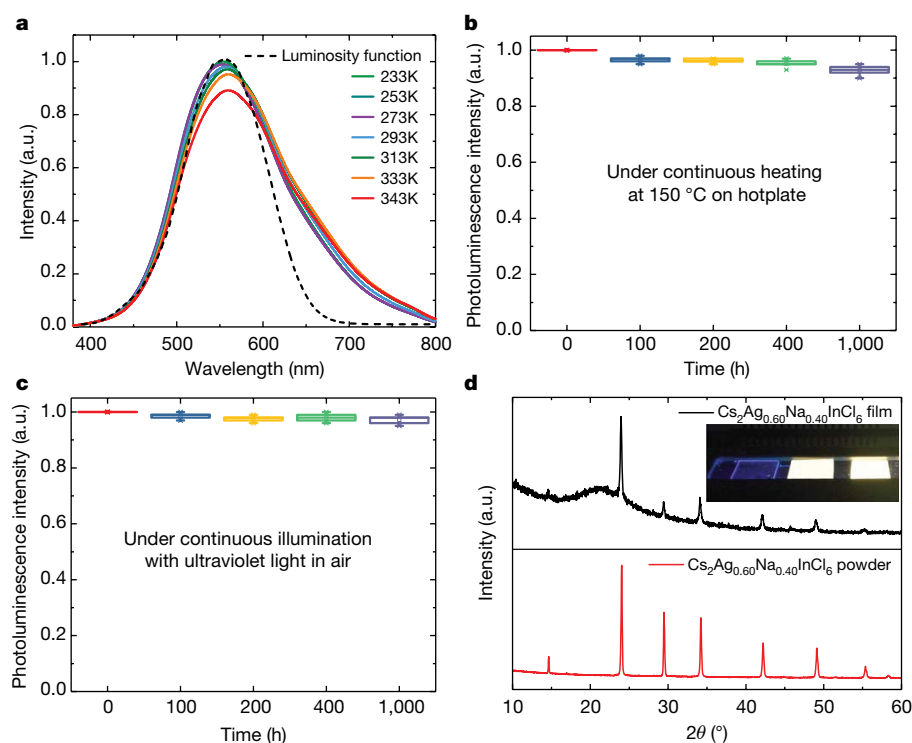


**Fig. 4 | White emission from  $\text{Cs}_2\text{Ag}_{1-x}\text{Na}_x\text{InCl}_6$ .** **a**, Luminosity function (dashed line) and photoluminescence spectra (solid lines) of  $\text{Cs}_2\text{Ag}_{0.60}\text{Na}_{0.40}\text{InCl}_6$  measured at different temperatures from 233 K to 343 K. **b**, Photoluminescence stability of  $\text{Cs}_2\text{Ag}_{0.60}\text{Na}_{0.40}\text{InCl}_6$  against continuous heating at  $150^\circ\text{C}$  on a hotplate, measured after cooling to room temperature. **c**, Operational stability of  $\text{Cs}_2\text{Ag}_{0.60}\text{Na}_{0.40}\text{InCl}_6$  down-conversion devices, measured in air without any encapsulation. The box plot shows the results for five different samples measured separately, with the box edges representing quartiles, the band inside the box showing the median and the end of the whiskers representing the minimum and maximum of the data. **d**, XRD patterns of a  $\text{Cs}_2\text{Ag}_{0.60}\text{Na}_{0.40}\text{InCl}_6$  film (black line) and powder (red line). The inset shows a 300-nm-thick quartz substrate and 500-nm-thick  $\text{Cs}_2\text{Ag}_{0.60}\text{Na}_{0.40}\text{InCl}_6$  films under 254-nm ultraviolet illumination.

white LED showed negligible degradation when operated at about  $5,000 \text{ cd m}^{-2}$  for over 1,000 h in air (Fig. 4c). This outstanding photometric performance, combined with its easy manufacture, indicate promise for white-phosphor applications.

The broadband emission associated with the STEs provides a new strategy to produce single-material-based, white-light electroluminescence. We thus fabricated prototype double-perovskite-based electroluminescence devices. XRD measurements confirmed the pure phase of the thermally evaporated  $\text{Cs}_2\text{Ag}_{0.60}\text{Na}_{0.40}\text{InCl}_6$  film, which showed bright and uniform warm-white photoluminescence under ultraviolet-lamp excitation (Fig. 4d). Our electroluminescence device demonstrated bias-insensitive broadband emission and a peak current efficiency of  $0.11 \text{ cd A}^{-1}$ , which was mainly limited by the low quality of the  $\text{Cs}_2\text{Ag}_{0.60}\text{Na}_{0.40}\text{InCl}_6$  films (Supplementary Figs. 15–17). Further research should focus on optimizing emitting-layer quality and device configuration to increase electroluminescence performance.

In summary, Na alloying into  $\text{Cs}_2\text{AgInCl}_6$  breaks the parity-forbidden transition and reduces its electronic dimensionality, leading to efficient white emission via radiative recombination of STEs. This white-light-emitting material also demonstrates outstanding stability and low-cost manufacture, indicating promise for solid-state lighting. We believe that halide double perovskites hold great potential for display and lighting applications and merit further study to realize their full potential.

## Online content

Any methods, additional references, Nature Research reporting summaries, source data, statements of data availability and associated accession codes are available at <http://sci-hub.tw/10.1038/s41586-018-0691-0>.

Received: 27 February 2018; Accepted: 31 August 2018;

Published online: 07 November 2018

- Sun, Y. et al. Management of singlet and triplet excitons for efficient white organic light-emitting devices. *Nature* **440**, 908–912 (2006).
- Tan, Z. K. et al. Bright light-emitting diodes based on organometal halide perovskite. *Nat. Nanotechnol.* **9**, 687–692 (2014).
- Cho, H. et al. Overcoming the electroluminescence efficiency limitations of perovskite light-emitting diodes. *Science* **350**, 1222–1225 (2015).
- Xiao, Z. et al. Searching for promising new perovskite-based photovoltaic absorbers: the importance of electronic dimensionality. *Mater. Horiz.* **4**, 206–216 (2017).
- Kojima, A., Teshima, K., Shirai, Y. & Miyasaka, T. Organometal halide perovskites as visible-light sensitizers for photovoltaic cells. *J. Am. Chem. Soc.* **131**, 6050–6051 (2009).
- Burschka, J. et al. Sequential deposition as a route to high-performance perovskite-sensitized solar cells. *Nature* **499**, 316–319 (2013).
- Lee, M. M., Teuscher, J., Miyasaka, T., Murakami, T. N. & Snaith, H. J. Efficient hybrid solar cells based on meso-superstructured organometal halide perovskites. *Science* **338**, 643–647 (2012).
- Yin, W. J., Shi, T. & Yan, Y. Unique properties of halide perovskites as possible origins of the superior solar cell performance. *Adv. Mater.* **26**, 4653–4658 (2014).
- Protesescu, L. et al. Nanocrystals of cesium lead halide perovskites ( $\text{CsPbX}_3$ , X=Cl, Br, and I): novel optoelectronic materials showing bright emission with wide color gamut. *Nano Lett.* **15**, 3692–3696 (2015).
- Zhou, Q. et al. In situ fabrication of halide perovskite nanocrystal embedded polymer composite films with enhanced photoluminescence for display backlights. *Adv. Mater.* **28**, 9163–9168 (2016).
- Wang, N. et al. Perovskite light-emitting diodes based on solution-processed self-organized multiple quantum wells. *Nat. Photon.* **10**, 699–704 (2016).
- Yuan, M. et al. Perovskite energy funnels for efficient light-emitting diodes. *Nat. Nanotechnol.* **11**, 872–877 (2016).
- Yang, X. et al. Efficient green light-emitting diodes based on quasi-two-dimensional composition and phase engineered perovskite with surface passivation. *Nat. Commun.* **9**, 570 (2018); correction **9**, 1169 (2018).
- Zhao, B. et al. High-efficiency perovskite-polymer bulk heterostructure light-emitting diodes. Preprint at <https://arxiv.org/abs/1804.09785> (2018).
- Dohner, R. E., Hoke, T. K. & Karunadasa, I. H. Self-assembly of broadband white-light emitters. *J. Am. Chem. Soc.* **136**, 1718–1721 (2014).
- Song, K. S. & Williams, R. T. *Self-Trapped Excitons* (Springer, New York, 2008).
- Smith, M. D. & Karunadasa, I. H. White-light emission from layered halide perovskites. *Acc. Chem. Res.* **51**, 619–627 (2018).
- Ueta, M., Kanzaki, H., Kobayashi, K., Toyozawa, Y. & Hanamura, E. in *Excitonic Processes in Solids* 309–369 (Springer, Berlin, Heidelberg, 1986).
- Dohner, R. E., Jaffe, A., Bradshaw, R. L. & Karunadasa, I. H. Intrinsic white-light emission from layered hybrid perovskites. *J. Am. Chem. Soc.* **136**, 13154–13157 (2014).
- Mao, L., Wu, Y., Stoumpos, C. C., Wasielewski, M. R. & Kanatzidis, M. G. White-light emission and structural distortion in new corrugated two-dimensional lead bromide perovskites. *J. Am. Chem. Soc.* **139**, 5210–5215 (2017).
- Zhou, C. et al. Luminescent zero-dimensional organic metal halide hybrids with near-unity quantum efficiency. *Chem. Sci.* **9**, 586–593 (2018).
- Volonakis, G. et al.  $\text{Cs}_2\text{InAgCl}_6$ : a new lead-free halide double perovskite with direct band gap. *J. Phys. Chem. Lett.* **8**, 772–778 (2017).
- Zhao, X. G. et al. Cu–In halide perovskite solar absorbers. *J. Am. Chem. Soc.* **139**, 6718–6725 (2017).
- Meng, W. et al. Parity-forbidden transitions and their impact on the optical absorption properties of lead-free metal halide perovskites and double perovskites. *J. Phys. Chem. Lett.* **8**, 2999–3007 (2017).
- Huang, K. & Rhys, A. Theory of light absorption and non-radiative transitions in F-centres. *Proc. R. Soc. Lond. A* **204**, 406–423 (1950).
- Lim, T.-W. et al. Insights into cationic ordering in Re-based double perovskite oxides. *Sci. Rep.* **6**, 19746 (2016).
- Maughan, A. E. et al. Defect tolerance to intolerance in the vacancy-ordered double perovskite semiconductors  $\text{Cs}_2\text{SnI}_6$  and  $\text{Cs}_2\text{TeI}_6$ . *J. Am. Chem. Soc.* **138**, 8453–8464 (2016).
- Yuan, Z. et al. One-dimensional organic lead halide perovskites with efficient bluish white-light emission. *Nat. Commun.* **8**, 14051 (2017).
- Kim, J.-H. et al. White electroluminescent lighting device based on a single quantum dot emitter. *Adv. Mater.* **28**, 5093–5098 (2016).
- Moser, F. & Lyu, S. Luminescence in pure and I-doped AgBr crystals. *J. Lumin.* **3**, 447–458 (1971).

**Acknowledgements** This work was financially supported by the National Natural Science Foundation of China (51761145048 and 61725401), the National Key R&D Program of China (2016YFB0700702, 2016YFA0204000 and 2016YFB0201204), the HUST Key Innovation Team for Interdisciplinary Promotion (2016JCTD111) and the Program for JLU Science and Technology Innovative Research Team. The calculation of broadband emission at the University of Toledo was supported by the Center for Hybrid Organic Inorganic Semiconductors for Energy (CHOISE), an Energy Frontier Research Center funded by the Office of Basic Energy Sciences, Office of Science within the US Department of Energy. The analysis of the electronic properties of halide double perovskites was funded by the Office of Energy Efficiency and Renewable Energy (EERE), US Department of Energy, under award number DE-EE0006712. Part of the code development was supported by the National Science Foundation under contract number DMR-1807818. Y.Y. acknowledges support from the Ohio Research Scholar Program. For the theoretical calculations we used the resources of the National Energy Research Scientific Computing Center, which is supported by the Office of Science of the US Department of Energy under contract number DE-AC02-05CH11231. Y.G. and J.E. acknowledge financial support by the Australian Research Council (DP150104483) and the use of instrumentation at the Monash Centre for Electron Microscopy. The authors from HUST thank the Analytical and Testing Center of HUST and the facility support of the Center for Nanoscale Characterization and Devices, WNLO. We also thank Z. Xiao for useful discussion about emission mechanisms and some XRD measurements, as well as T. Zhai, H. Song, Y. Zhou, H. Han, X. Lu and L. Xu for providing access to some facilities.

**Reviewer information** Nature thanks C. C. Stoumpos and the other anonymous reviewer(s) for their contribution to the peer review of this work.

**Author contributions** J.T. conceived the idea and guided the whole project. J. Luo, S.L. and J. Liu designed and performed most of the experiments and analysed the data; X.W. performed most of the theoretical calculations and analysis (GW-BSE, STE, photoluminescence) under the guidance of Y.Y.; S.L. discovered the phosphor; L.Y. contributed in electroluminescence device optimization; L.G. carried out transient-absorption experiments; M.L. assisted in data analysis and photoluminescence measurements; Y.G. and J.E. carried out the electron microscopy measurements and analysed the results; Y.F. and L.Z. simulated the band alignment and the contour plots of the valence-band maximum and conduction-band maximum charge densities; C.Z. and S.J. provided some optical measurements; Q.D., F.M., L.W., W.L. and J.H. helped in the PLQY measurement and electroluminescence device fabrication; G.N. was involved in data analysis and experimental design; J.W. contributed to DFT calculations, Y.Y. helped in manuscript writing; J. Luo, X.W., E.H.S. and J.T. wrote the paper; all authors commented on the manuscript.

**Competing interests** The authors declare no competing interests.

## Additional information

**Extended data** is available for this paper at <https://doi.org/10.1038/s41586-018-0691-0>.

**Supplementary information** is available for this paper at <https://doi.org/10.1038/s41586-018-0691-0>.

**Reprints and permissions information** is available at <http://www.nature.com/reprints>.

**Correspondence and requests for materials** should be addressed to Y.Y. or J.T.

**Publisher's note:** Springer Nature remains neutral with regard to jurisdictional claims in published maps and institutional affiliations.

## METHODS

**Materials.** Caesium chloride (CsCl, 99.99%), silver chloride (AgCl, 99.99%), sodium chloride (NaCl, 99.99%), lithium chloride (LiCl, 99.9%), anhydrous indium chloride (InCl<sub>3</sub>, 99.999%), anhydrous bismuth chloride (BiCl<sub>3</sub>, 99.999%), anhydrous antimony chloride (SbCl<sub>3</sub>, 99.99%), zinc acetate dehydrate (Zn(CH<sub>3</sub>COO)<sub>2</sub>·2H<sub>2</sub>O >98%), tetramethylammonium hydroxide (TMAH, 98%) and polyethylenimine (PEIE) were purchased from Sigma Aldrich. Molybdenum oxide (MoO<sub>3</sub>, 99%) and 4,4'-cyclohexylidenebis[*N,N*-bis(4-methylphenyl)benzamine] (TAPC, 99%) were purchased from Guangdong Aglaia Optoelectronic Materials Company. Hydrochloric acid, ethanol, acetone, isopropanol, ethyl acetate, 1-butanol and dimethyl sulfoxide (DMSO, 99%) were purchased from Sinopharm Chemical Reagent Company. Patterned indium tin oxide (ITO) glass substrates (sheet resistance, 15 Ω sq<sup>-1</sup>) were purchased from Guangdong Xiangcheng Technology Company. All materials were used as received.

**Synthesis of alloyed double-perovskite materials.** Because double perovskites are generally impurity-sensitive, a Teflon autoclave was soaked overnight with aqua regia and high-purity raw materials were used. Then, 1 mmol anhydrous InCl<sub>3</sub>, 0.005 mmol anhydrous BiCl<sub>3</sub> and 2 mmol CsCl were first dissolved in 10 ml of a 10 M HCl solution in a 25-ml Teflon autoclave. Then *x* mmol of AgCl and 1−*x* mmol of NaCl were added and the solution was heated at 180 °C for 12 h in a stainless-steel Parr autoclave. The solution was then steadily cooled to 50 °C at a speed of 3 °C h<sup>-1</sup> (the cooling process was key in determining the PLQY of the products). The as-prepared crystals were then filtered out, washed with isopropanol and dried in a furnace at 60 °C. Na-doped Cs<sub>2</sub>AgSbCl<sub>6</sub> was synthesized by substituting the InCl<sub>3</sub> with SbCl<sub>3</sub>, and Li-doped Cs<sub>2</sub>AgInCl<sub>6</sub> was obtained by mixing 20 mmol LiCl with 1 mmol Cs<sub>2</sub>AgInCl<sub>6</sub> in a 25-ml Teflon autoclave containing 4 ml of a 10 M HCl solution, and then following exactly the same procedure as for the Cs<sub>2</sub>Ag<sub>*x*</sub>Na<sub>1−*x*</sub>InCl<sub>6</sub> synthesis.

**Characterization and calibration of the PLQY of Cs<sub>2</sub>Ag<sub>*x*</sub>Na<sub>1−*x*</sub>InCl<sub>6</sub>.** The PLQY was measured using an absolute photoluminescence measurement system (Hamamatsu Quantaurus-QY) at Tsinghua University. The excitation wavelength was 365 nm, and the step increments and integration time were 1 nm and 0.5 s per data point, respectively. Commercial YAG:Ce<sup>3+</sup> powder purchased from Hunan LED Company with a standard PLQY (80%–85%, 460 nm excitation) was used to calibrate the system.

**Electroluminescence device fabrication.** Colloidal ZnO nanocrystals were synthesized following a published procedure<sup>31</sup>. Patterned indium-doped ITO substrates were cleaned by sequential sonication in acetone, ethanol and deionized water, for 30 min in each bath. After drying, solutions of PEIE in isopropanol (0.1 wt%) were spin-coated onto the ITO substrates at 5,000 r.p.m. for 60 s, followed by a layer of ZnO nanocrystals spun at 3,000 r.p.m. for 60 s, and a further PEIE layer (0.1 wt% in 2-methoxyethanol), spin-coated at 5,000 r.p.m. for 60 s. The Cs<sub>2</sub>Ag<sub>0.60</sub>Na<sub>0.40</sub>InCl<sub>6</sub> film was deposited by thermal evaporation of CsCl, AgCl, NaCl, InCl<sub>3</sub> and BiCl<sub>3</sub> in separate crucibles at a stoichiometric molar ratio of 2:0.6:0.4:1:~0.005. The evaporation rate was monitored by a quartz microbalance. After the pressure of the evaporator chamber (Fangsheng Technology, OMV-FS300) was pumped down to 6 × 10<sup>-6</sup> mTorr, one precursor was heated slowly to achieve a desirable deposition rate (CsCl, 0.10–0.20 Å s<sup>-1</sup>; NaCl, 0.01–0.03 Å s<sup>-1</sup>; AgCl, 0.05–0.10 Å s<sup>-1</sup>; InCl<sub>3</sub>, 0.10–0.20 Å s<sup>-1</sup>; BiCl<sub>3</sub>, 0.01 Å s<sup>-1</sup>). The shutter was then manually opened until a certain thickness was deposited. The evaporation sequence was CsCl, InCl<sub>3</sub>, BiCl<sub>3</sub>, NaCl and AgCl. Then, the Cs<sub>2</sub>Ag<sub>0.60</sub>Na<sub>0.40</sub>InCl<sub>6</sub> film was exposed to air for 5 min and further annealed at 150 °C in N<sub>2</sub> for 5 min to promote crystallization. Afterwards, 40-nm-thick TAPC layers were deposited at a speed of 0.10–0.20 Å s<sup>-1</sup>, followed by the deposition of the MoO<sub>3</sub>/Al electrode to complete the device (device area, 4 mm<sup>2</sup>).

**Material characterization.** Powder XRD measurements were performed by grinding Cs<sub>2</sub>Ag<sub>*x*</sub>Na<sub>1−*x*</sub>InCl<sub>6</sub> crystals into fine powders in a mortar, using a Philips X'pert pro MRD diffractometer with Cu Kα radiation. High-resolution XRD measurements were conducted on a powder diffractometer (D8 ADVANCE, Bruker) using a Cu Kα rotating anode. The absorption and reflectance spectra were measured on an ultraviolet–visible spectrophotometer (PerkinElmer Instruments, Lambda 950) with an integrating sphere, which was calibrated by measuring a reference material (MgO powder) at the same time. The photoluminescence and PLE measurements were carried out using an Edinburgh Instruments Ltd UC920 spectrometer. The temperature-dependent photoluminescence spectra were measured using a Horiba Jobin Yvon LabRAM HR800 Raman spectrometer excited by a 325-nm-wavelength He–Cd laser and at a temperature ranging from 80 to 500 K, achieved using a liquid-nitrogen cooler. The intensity-dependent photoluminescence measurement was also carried out using a picosecond-pulse diode laser (Light Conversion, Pharos) with 365-nm output wavelength and 50-ps pulse width, and the pulse intensity was monitored by a power meter (Ophir PE10BF-C). The power density was controlled by neutral-density filters (Light Conversion, Pharos). The photoluminescence lifetime measurement was performed using time-correlated single-photon counter technology. The excitation beam was a picosecond-pulse diode

laser (Light Conversion, Pharos) with 365-nm output wavelength and 50-ps pulse width. For the transient-absorption measurement, an amplified Yb:KGW laser (Light Conversion, Pharos) with 5-kHz repetition rate was used to generate femtosecond-laser pulses (pump wavelength, 325 nm; intensity, 4 μJ cm<sup>-2</sup>). A crystal with a size of about 0.2 × 1.0 × 1.0 mm<sup>3</sup> was placed on the glass substrate during the measurement. ICP-OES measurements were carried out using a Perkin Elmer Optima 7300DV spectrometer with the Cs<sub>2</sub>Ag<sub>*x*</sub>Na<sub>1−*x*</sub>InCl<sub>6</sub> powders dissolved in HCl. Thermal gravimetric analysis were performed with a PerkinElmer Diamond TG/DTA6300 system at a heating rate of 10 °C min<sup>-1</sup> from room temperature to 800 °C in N<sub>2</sub> flow using an alumina crucible. A Cs<sub>2</sub>Ag<sub>0.60</sub>Na<sub>0.40</sub>InCl<sub>6</sub> thin film fabricated by thermal evaporation was characterized by scanning electron microscopy (FEI Nova NanoSEM450, without Pt coating), ultraviolet photoemission spectroscopy (Specs UVLS, He I excitation, 21.2 eV; referenced to the Fermi edge of argon-etched gold). Stability against heat was measured by simply putting the powders on a 150 °C hotplate in N<sub>2</sub>, and the photoluminescence intensity was measured after a certain time interval. We note that all measurements were performed on powder and crystals, except for the electroluminescence measurements, which were made on films.

**Transmission electron microscopy analysis.** Transmission electron microscopy (TEM) specimens were prepared by crushing the as-grown single crystals and then drop-casting them onto a TEM copper grid covered by an ultrathin carbon film. TEM characterization was carried out on a JEOL 2100F TEM with a field-emission gun operating at 200 kV at the Monash Centre for Electron Microscopy (MCEM). Low-dose selected-area electron diffraction and scanning electron nanobeam diffraction were performed to avoid beam damage. Using a nominal current density of 2 pA cm<sup>-2</sup>, no change in lattice parameters was observed after several minutes' exposure. For the scanning electron nanobeam diffraction measurement, a step size of 5 nm was used and a dataset of 10 × 10 diffraction patterns of (2,048 pixels) × (2,048 pixels) was collected from a square region of 50 × 50 nm<sup>2</sup>. We deployed a digital micrograph script for automatic control of the scanning coils and pattern acquisition, developed by J. M. Zuo's group at the University of Illinois at Urbana-Champaign.

**First-principles density functional theory, many-body perturbation theory and BSE calculations.** Density functional theory, GW and BSE calculations were performed using the VASP code<sup>32,33</sup> with projector augmented-wave (PAW)<sup>34</sup> potentials. A kinetic energy cutoff of 520 eV and  $\Gamma$ -centred 4 × 4 × 4 *k*-mesh were employed. Because the band gaps of both Cs<sub>2</sub>AgInCl<sub>6</sub> and Cs<sub>2</sub>NaInCl<sub>6</sub> were found to be sensitive to the bond length, we used the more accurate PBE0<sup>35</sup> functional to relax the atomic coordinates with a force tolerance of 0.01 eV Å<sup>-1</sup> while keeping the lattice parameters fixed at their experimental values. With the relaxed coordinates, GW calculations were performed using the PBE<sup>36</sup> wavefunction. Partial self-consistency on Green's function only—the GW<sub>0</sub> scheme—was adopted. For the GW calculations, an energy cutoff of 200 eV for the response function, 200 real frequency grids for the dielectric function and 1,000 bands were used. The results were further extrapolated to infinite-basis sets and a number of bands<sup>37</sup>. GW band structures were obtained using Wannier interpolation with the wannier90 code<sup>38</sup>. BSE calculations were performed using the GW quasiparticle energies. The number of occupied/virtual states used for Cs<sub>2</sub>AgInCl<sub>6</sub> and Cs<sub>2</sub>NaInCl<sub>6</sub> were 2/2 and 24/4, respectively, to achieve convergence of the several low-lying exciton states. The exciton binding energies were extrapolated to infinitely dense *k*-meshes. For a finer *k*-mesh, GW calculations are computationally prohibitive. We used Wannier interpolation to interpolate the GW quasiparticle energies and model the dielectric function<sup>39</sup>  $\epsilon_q$ , which was fitted from the value obtained with a coarser grid to interpolate the dielectric function ( $\epsilon_q = 1 + [(\epsilon_\infty - 1)^{-1} + aq^2 + bq^4]^{-1}$ , where  $\epsilon_\infty$  is the static dielectric constant, *q* is the wave vector, and *a* and *b* are fitting parameters).

**STE calculation.** To study the STE properties, we used the restricted open-shell Kohn–Sham (ROKS) theory<sup>40–42</sup>, as implemented in the *cp2k* code<sup>43</sup>. A supercell with a single  $\Gamma$  point was used in the calculation. The double-zeta valence polarization molecularly optimized basis sets<sup>44</sup>, PBE exchange–correlation functional and Goedecker–Teter–Hutter pseudopotentials<sup>45</sup> were used. Energy cutoffs of 300 Ry and 1,200 Ry (1 rydberg, 1 Ry = 13.605 eV) were used for Cs<sub>2</sub>AgInCl<sub>6</sub> and Cs<sub>2</sub>NaInCl<sub>6</sub>, respectively. The delocalization error of the PBE functional was removed using the scaled Perdew–Zunger self-interaction correction<sup>46,47</sup> only on the unpaired electrons<sup>48</sup>. The scaling parameter  $\alpha$  of the Hartree energy was fitted to reproduce the exciton binding energies calculated by the GW–BSE approach. The exciton binding energy within the ROKS framework is calculated as  $E_b = E_g - (S_1 - E_0)$ , where *S*<sub>1</sub> and *E*<sub>0</sub> are the first excited singlet-state and ground-state energies, respectively. We obtained  $\alpha = 0.30$  and  $\alpha = 0.34$  for Cs<sub>2</sub>AgInCl<sub>6</sub> and Cs<sub>2</sub>NaInCl<sub>6</sub>, respectively. Because the present self-interaction correction scheme is not meant to correct the bandgap, the excited-state curves in the configuration coordinate diagrams were shifted by aligning the free-exciton energy with that from the GW–BSE calculations. A supercell with a size of 21.0 × 21.0 × 21.0 Å<sup>3</sup> was found enough to obtain convergence of both the free exciton and the STE of

Cs<sub>2</sub>NaInCl<sub>6</sub>. However, for Cs<sub>2</sub>AgInCl<sub>6</sub>, owing to the small effective mass of the electron, a supercell with a size as large as 41.9 × 41.9 × 41.9 Å<sup>3</sup> is needed. For a completely delocalized state, the self-interaction correction is zero; hence, we neglected the self-interaction correction on the electron wavefunction of the STE in Cs<sub>2</sub>AgInCl<sub>6</sub>. This can safely reduce the supercell size to only 20.9 × 20.9 × 20.9 Å<sup>3</sup>. For the alloyed double perovskites, we used a supercell of 21.0 × 21.0 × 21.0 Å<sup>3</sup> and α = 0.34.

#### Configuration coordinate diagram and photoluminescence spectra calculation.

The configuration coordinate (Q) diagram was constructed by linearly interpolating the coordinates between the free-exciton and STE configurations and then calculating both the ground-state and excited-state energies at each coordinate. The coordinate difference between the free-exciton and STE configurations is  $\Delta Q = \sqrt{\sum_{\kappa,i} M_{\kappa} (R_{\kappa,i}^e - R_{\kappa,i}^g)^2}$ , where κ denotes the atom, i = (x, y, z), M is the atomic mass and R are the atomic coordinates with e and g for the excited and ground state, respectively. The calculated ΔQ is 4.35 Å AMU<sup>1/2</sup> and 9.16 Å AMU<sup>1/2</sup>, respectively, for Cs<sub>2</sub>AgInCl<sub>6</sub> and Cs<sub>2</sub>NaInCl<sub>6</sub>. The coordinate Q was linearly interpolated between 0 and ΔQ. The phonon frequency Ω was obtained by a third-order polynomial fit ((1/2)Ω<sup>2</sup>Q<sup>2</sup> + λQ<sup>3</sup>; λ is a fitting parameter) of the excited- or ground-state curve. The normalized photoluminescence intensity in the leading order can be written as<sup>49</sup>  $I(h\nu) = C\nu^x A(h\nu)$  (x = 3 for dipole-allowed transition, x = 5 for dipole-forbidden transition), where hν is the photon energy and C is the normalization factor, which includes the transition dipole moments for dipole-allowed transitions, or the magnetic dipole moments and electric quadrupole moments for dipole-forbidden transitions. A is the normalized spectral function, under the Franck–Condon approximation:

$$A(h\nu) = \sum_{m,n} w_m(T) |\langle \chi_{gn} | \chi_{em} \rangle|^2 \delta(E_{ZPL} + \hbar\omega_m - \hbar\omega_n - h\nu) \quad (1)$$

$w_m(T)$  is the thermal occupation factor of the excited-state phonons with energy  $\hbar\omega_m = (m)\hbar\Omega_m$ , where Ω<sub>m</sub> is the phonon frequency, m is the corresponding quantum number, n denotes the related ground-state quantity, T is the temperature and k<sub>B</sub> is the Boltzmann constant. E<sub>ZPL</sub> is the zero-phonon line energy, which is the energy difference between the minima of the excited- and ground-state curves plus the zero-point energy difference, (1/2)ħ(Ω<sub>e</sub> – Ω<sub>g</sub>).  $\chi_{em}$  and  $\chi_{gn}$  are the harmonic phonon wavefunctions of the excited and ground states, respectively. The Franck–Condon factors  $|\langle \chi_{gn} | \chi_{em} \rangle|^2$  were calculated by the recurrence method<sup>50</sup>. The δ function in equation (1) was replaced by the Lorentzian with a broadening parameter of 0.03 eV, which is around the phonon cutoff frequency of Cs<sub>2</sub>AgInCl<sub>6</sub> (Extended Data Fig. 2).

**LED devices on ultraviolet chips.** GaN-based ultraviolet chips (14 W output, 365–370 nm peak emission) were purchased from Taiwan Epileds Company. The Cs<sub>2</sub>Ag<sub>0.60</sub>Na<sub>0.40</sub>InCl<sub>6</sub> crystals were ball-milled into fine powder, and the powder was painted onto the commercial chips without encapsulation. The LEDs were driven by a Keithley 2400 source meter, and the emission spectra and intensity were recorded by a Photo Research SpectraScan PR655 photometer. For the device stability test, the LED was continuously powered by a Keithley 2400 source meter at a fixed current, and the initial brightness was set at about 5,000 cd m<sup>-2</sup>. The device performance was monitored after a certain time interval.

**Electroluminescence device performance measurement.** The density–voltage and luminance–voltage characteristics and the electroluminescence spectra of the devices were collected by a Photo Research SpectraScan PR655 photometer and a Keithley 2400 source meter constant-current source. All the experiments were carried out at room temperature under ambient conditions in the dark.

**Calculation and comparison of Huang–Rhys factors.** In principle, the Huang–Rhys factor (S) reflects how strongly electrons couple to phonons and can be obtained by fitting the temperature-dependent full-width at half-maxima (FWHM) of photoluminescence peaks using the following equation<sup>51</sup>

$$\text{FWHM} = 2.36\sqrt{S}\hbar\omega_{\text{phonon}} \sqrt{\cot\left(\frac{\hbar\omega_{\text{phonon}}}{2k_B T}\right)} \quad (2)$$

where  $\hbar\omega_{\text{phonon}}$  is the phonon frequency. For Cs<sub>2</sub>AgInCl<sub>6</sub>, S and  $\hbar\omega_{\text{phonon}}$  are calculated as 38.7 and 20.1 meV, respectively, in good agreement with our simulation results (37 and 17.4 meV). Extended Data Table 1 lists the S values of a few representative compounds—we note that the Huang–Rhys factor of nanomaterials is generally higher than that of their bulk counterparts because of quantum confinement<sup>52</sup>. The Huang–Rhys factor of Cs<sub>2</sub>AgInCl<sub>6</sub> is 38.7, which is larger than that of many common emitters, such as CdSe<sup>53</sup>, ZnSe<sup>54</sup> and CsPbBr<sub>3</sub><sup>55</sup>, indicating the easy formation of STEs in Cs<sub>2</sub>AgInCl<sub>6</sub>. For comparison, formation of STEs is also found in materials with high Huang–Rhys factors<sup>56</sup>, such as Cs<sub>3</sub>Sb<sub>2</sub>I<sub>9</sub>, Cs<sub>3</sub>Bi<sub>2</sub>I<sub>9</sub> and Rb<sub>3</sub>Sb<sub>2</sub>I<sub>9</sub>. However, for efficient STE emission, S should not be overly large, because otherwise the excited-state energy would be dissipated by phonons, as is the case in Cs<sub>2</sub>NaInCl<sub>6</sub>. This is because S also influences photoluminescence

emission through the Franck–Condon factor, as described by equation (1). If we assume that the ground and excited states have similar phonon frequencies, the Franck–Condon factor (F, at zero temperature) can be simplified as

$$F = |\langle \chi_n | \chi_m \rangle|^2 = \frac{e^{-S} S^n}{n!} \quad (3)$$

The photoluminescence peak appears at  $n \approx S$ , so

$$F_{\text{max}} = \frac{e^{-S} S^S}{S!} \quad (4)$$

which is a monotonically decreasing function of S. Because the photoluminescence intensity is positively correlated with S, the larger the S, the smaller the radiative rate and the lower the emission efficiency. Thereby, the S value could potentially serve as the figure of merit for the design of efficient emission from STEs. The ideal value of the Huang–Rhys parameter should be intermediate for efficient STE emitters.

**Mechanistic study of Bi<sup>3+</sup> doping.** Extended Data Fig. 6 provides information about the effect of Bi<sup>3+</sup> incorporation on the PLQY improvement. For a Bi-doped Cs<sub>2</sub>AgInCl<sub>6</sub> sample, the XRD measurement revealed smaller FWHM (from 0.058° to 0.034°) of the diffraction patterns, and the optical measurement demonstrated diminished sub-bandgap absorption after 400 nm and increased photoluminescence lifetime—from 2,971 ns (70%) to 5,989 ns (97%). Because an In<sup>3+</sup> vacancy is a deep defect in Cs<sub>2</sub>AgInCl<sub>6</sub>, and isovalent doping helps to reduce vacancy defects in perovskite, we believe that Bi doping passivates defects and suppresses non-radiative recombination loss. Additionally, the theoretical simulation indicated that Bi doping introduces a shallow state right above the valence-band maximum and forms nanoelectronic domains in the matrix that concentrate holes. The holes finally relax to Ag sites through Bi 6s/Ag 4d orbital hybridization and lattice interaction, promoting exciton localization, just like I-doped AgBr for STE emission. Therefore, Bi doping improves crystal quality and promotes radiative recombination, enhancing the PLQY.

**Code availability.** The customized codes required for STE calculation with cp2k and the Python script used to calculate the Franck–Condon factors and luminescence spectrum are freely available at <https://github.com/wxiaom86>.

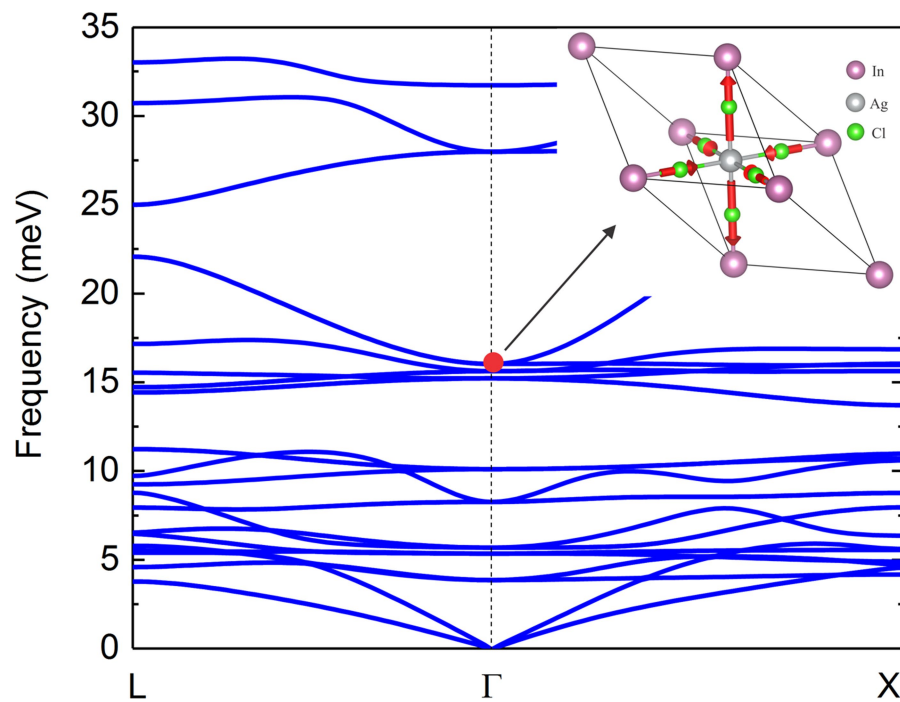
#### Data availability

The datasets analysed during the study are available from the corresponding authors upon request.

- Dai, X. et al. Solution-processed, high-performance light-emitting diodes based on quantum dots. *Nature* **515**, 96–99 (2014).
- Kresse, G. & Furthmüller, J. Efficient iterative schemes for ab initio total-energy calculations using a plane-wave basis set. *Phys. Rev. B* **54**, 11169–11186 (1996).
- Kresse, G. & Furthmüller, J. Efficiency of ab initio total energy calculations for metals and semiconductors using a plane wave basis set. *Comput. Mater. Sci.* **6**, 15 (1996).
- Blöchl, P. E. Projector augmented-wave method. *Phys. Rev. B* **50**, 17953–17979 (1994).
- Perdew, J. P., Ernzerhof, M. & Burke, K. Rationale for mixing exact exchange with density functional approximations. *J. Chem. Phys.* **105**, 9982–9985 (1996).
- Perdew, J., Burke, K. & Ernzerhof, M. Generalized gradient approximation made simple. *Phys. Rev. Lett.* **77**, 3865–3868 (1996).
- Klimeš, J., Kaltak, M. & Kresse, G. Predictive GW calculations using plane waves and pseudopotentials. *Phys. Rev. B* **90**, 075125 (2014).
- Mostofi, A. A. et al. wannier90: a tool for obtaining maximally-localised Wannier functions. *Comput. Phys. Commun.* **178**, 685–699 (2008).
- Cappellini, G. et al. Model dielectric function for semiconductors. *Phys. Rev. B* **47**, 9892 (1993).
- Kowalczyk, T., Tsuchimochi, T., Chen, P. T., Top, L. & Van Voorhis, T. Excitation energies and Stokes shifts from a restricted open-shell Kohn–Sham approach. *J. Chem. Phys.* **138**, 164101 (2013).
- Filatov, M. & Shaik, S. A spin-restricted ensemble-referenced Kohn–Sham method and its application to diradicaloid situations. *Chem. Phys. Lett.* **304**, 429–437 (1999).
- Frank, I., Hutter, J., Marx, D. & Parrinello, M. Molecular dynamics in low-spin excited states. *J. Chem. Phys.* **108**, 4060–4069 (1998).
- Hutter, J., Iannuzzi, M., Schiffmann, F. & Vandevondele, J. Cp2k: atomistic simulations of condensed matter systems. *Wiley Interdiscip. Rev. Comput. Mol. Sci.* **4**, 15–25 (2014).
- Vandevondele, J. & Hutter, J. Gaussian basis sets for accurate calculations on molecular systems in gas and condensed phases. *J. Chem. Phys.* **127**, 114105 (2007).
- Goedecker, S., Teter, M. & Hutter, J. Separable dual-space Gaussian pseudopotentials. *Phys. Rev. B* **54**, 1703–1710 (1996).
- Perdew, J. P. & Zunger, A. Self-interaction correction to density-functional approximations for many-electron systems. *Phys. Rev. B* **23**, 5048–5079 (1981).

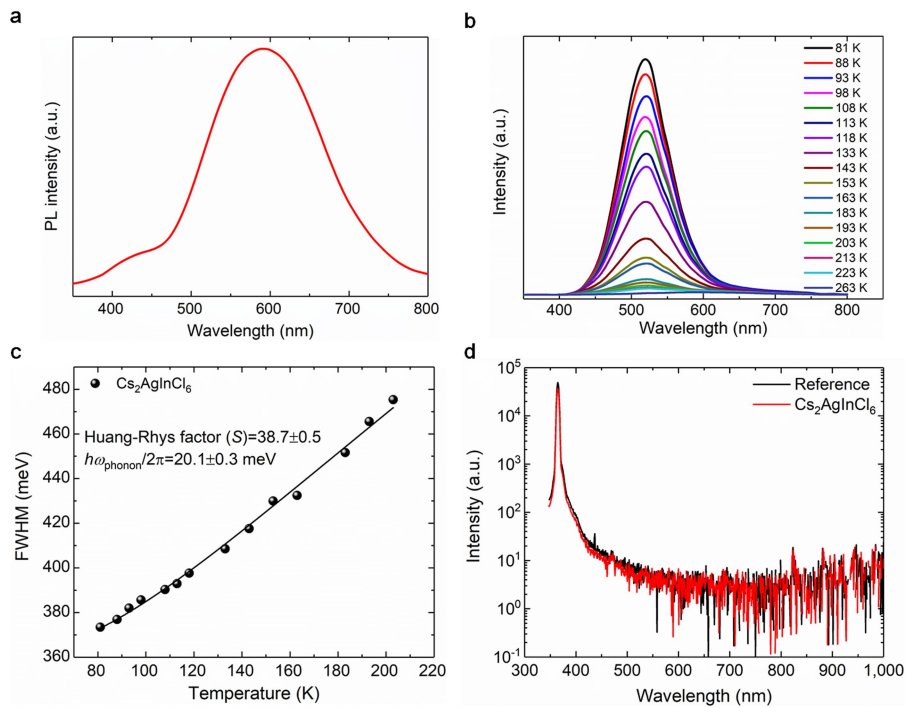
47. VandeVondele, J. & Sprik, M. A molecular dynamics study of the hydroxyl radical in solution applying self-interaction-corrected density functional methods. *Phys. Chem. Chem. Phys.* **7**, 1363 (2005).
48. d'Avezac, M., Calandra, M. & Mauri, F. Density functional theory description of hole-trapping in SiO<sub>2</sub>: a self-interaction-corrected approach. *Phys. Rev. B* **71**, 205210 (2005).
49. Alkauskas, A., Lyons, J. L., Steiauf, D. & Van De Walle, C. G. First-principles calculations of luminescence spectrum line shapes for defects in semiconductors: the example of GaN and ZnO. *Phys. Rev. Lett.* **109**, 267401 (2012).
50. Ruhoff, P. T. Recursion relations for multi-dimensional Franck–Condon overlap integrals. *Chem. Phys.* **186**, 355–374 (1994).
51. Stadler, W. et al. Optical investigations of defects in Cd<sub>1-x</sub>Zn<sub>x</sub>Te. *Phys. Rev. B* **51**, 10619 (1995).
52. Nandakumar, P. et al. Optical absorption and photoluminescence studies on CdS quantum dots in Nafion. *J. Appl. Phys.* **91**, 1509–1514 (2002).
53. Türck, V. et al. Effect of random field fluctuations on excitonic transitions of individual CdSe quantum dots. *Phys. Rev. B* **61**, 9944 (2000).
54. Zhao, H. et al. Energy-dependent Huang–Rhys factor of free excitons. *Phys. Rev. B* **68**, 125309 (2003).
55. Lao, X. et al. Luminescence and thermal behaviors of free and trapped excitons in cesium lead halide perovskite nanosheets. *Nanoscale* **10**, 9949–9956 (2018).
56. McCall, K. M. et al. Strong electron–phonon coupling and self-trapped excitons in the defect halide perovskites A<sub>3</sub>M<sub>2</sub>I<sub>9</sub> (A=Cs, Rb; M=Bi, Sb). *Chem. Mater.* **29**, 4129–4145 (2017).
57. Leung, C. H. & Song, K. S. On the luminescence quenching of F centers in alkali halides. *Solid State Commun.* **33**, 907 (1980).
58. Mulazzi, E. & Terzi, N. Evaluation of the Huang–Rhys factor and the half-width of F-band in KCl and NaCl crystals. *J. Phys. Colloq.* **28**, 49–54 (1967).
59. Schulz, M. et al. Intensity dependent effects in silver chloride: bromine-bound exciton and biexciton states. *Phys. Status Solidi B* **177**, 201–212 (1993).
60. Andrews, L. J. et al. Thermal quenching of chromium photoluminescence in ordered perovskites. I. Temperature dependence of spectra and lifetimes. *Phys. Rev. B* **34**, 2735 (1986).





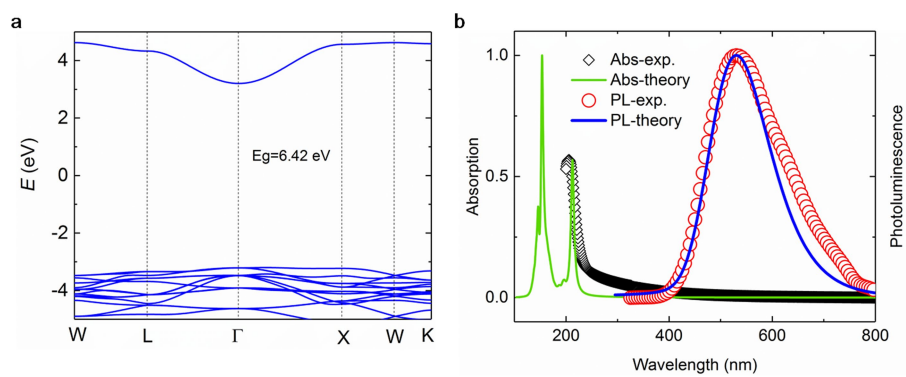
**Extended Data Fig. 1 | Phonon band structure of Cs<sub>2</sub>AgInCl<sub>6</sub> and the zone-centre Jahn-Teller phonon mode (inset).** The phonon band structure was calculated by the finite-difference method with the supercell approach. The consistency of the displacement pattern of the phonon eigenvector with that of the lattice distortion during STE formation, as

well as the consistency of the phonon eigenfrequency with the phonon frequency fitted from the configuration coordinate diagram, confirm that the Jahn-Teller phonon mode coupled with the photoexcited excitons is responsible for the STE formation in Cs<sub>2</sub>AgInCl<sub>6</sub>.



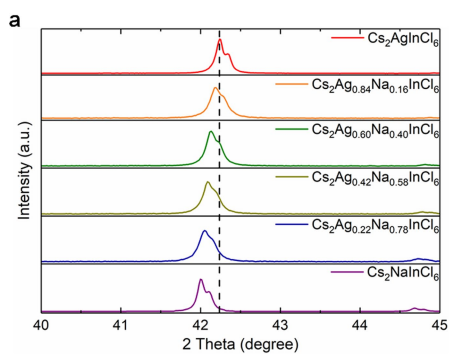
**Extended Data Fig. 2 | Emission characterization of pure  $\text{Cs}_2\text{AgInCl}_6$ .** **a**, The broad photoluminescence (PL) spectrum of  $\text{Cs}_2\text{AgInCl}_6$  measured at room temperature. **b**, Temperature-dependent photoluminescence spectra of pure  $\text{Cs}_2\text{AgInCl}_6$ . **c**, Fitting results of the FWHM as a function

of temperature. We note that we used a relatively low-temperature region to avoid the influence of defect-assisted emission. **d**, The PLQY of  $\text{Cs}_2\text{AgInCl}_6$ . The reference was measured in an integrating sphere with a blank quartz plate.



**Extended Data Fig. 3 | Electronic and optical properties of  $\text{Cs}_2\text{NaInCl}_6$ .** **a**, GW-calculated band structure. The GW bandgap is 6.42 eV. The lowest exciton, with a binding energy of 0.8 eV, is dark. The first bright exciton

has a binding energy of 0.44 eV. **b**, Calculated optical absorption ('Abs-theory') and photoluminescence ('PL-theory') spectra are compared with experimental results ('Abs-exp.' and 'PL-exp.').



**Extended Data Fig. 4 | Alloy behaviour of  $\text{Cs}_2\text{Ag}_x\text{Na}_{1-x}\text{InCl}_6$ .** **a**, XRD patterns of  $\text{Cs}_2\text{Ag}_x\text{Na}_{1-x}\text{InCl}_6$ , shifted to lower degrees with increasing sodium substitution (theta, diffraction angle). **b**, Refined lattice parameter, plotted as a function of the nominal  $x$  in  $\text{Cs}_2\text{Ag}_x\text{Na}_{1-x}\text{InCl}_6$ , showing a linear increase with increased sodium substitution (see Supplementary

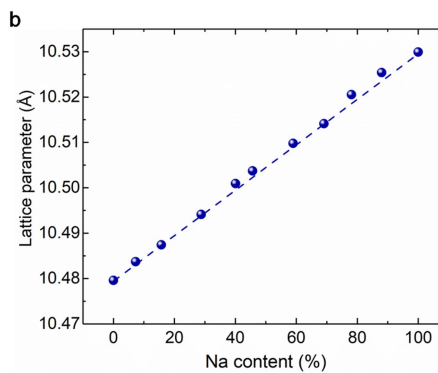
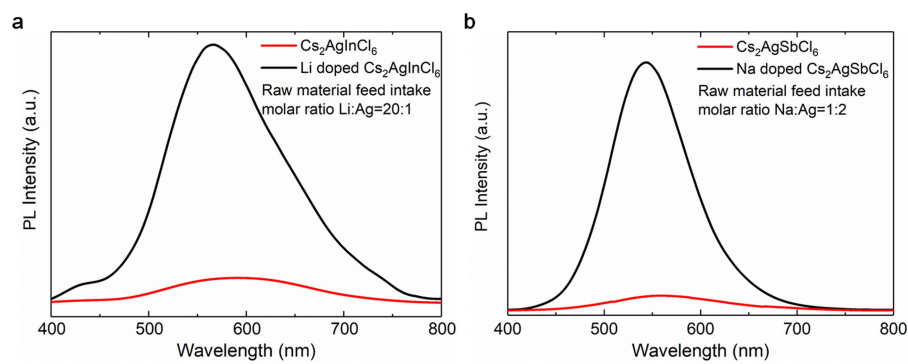
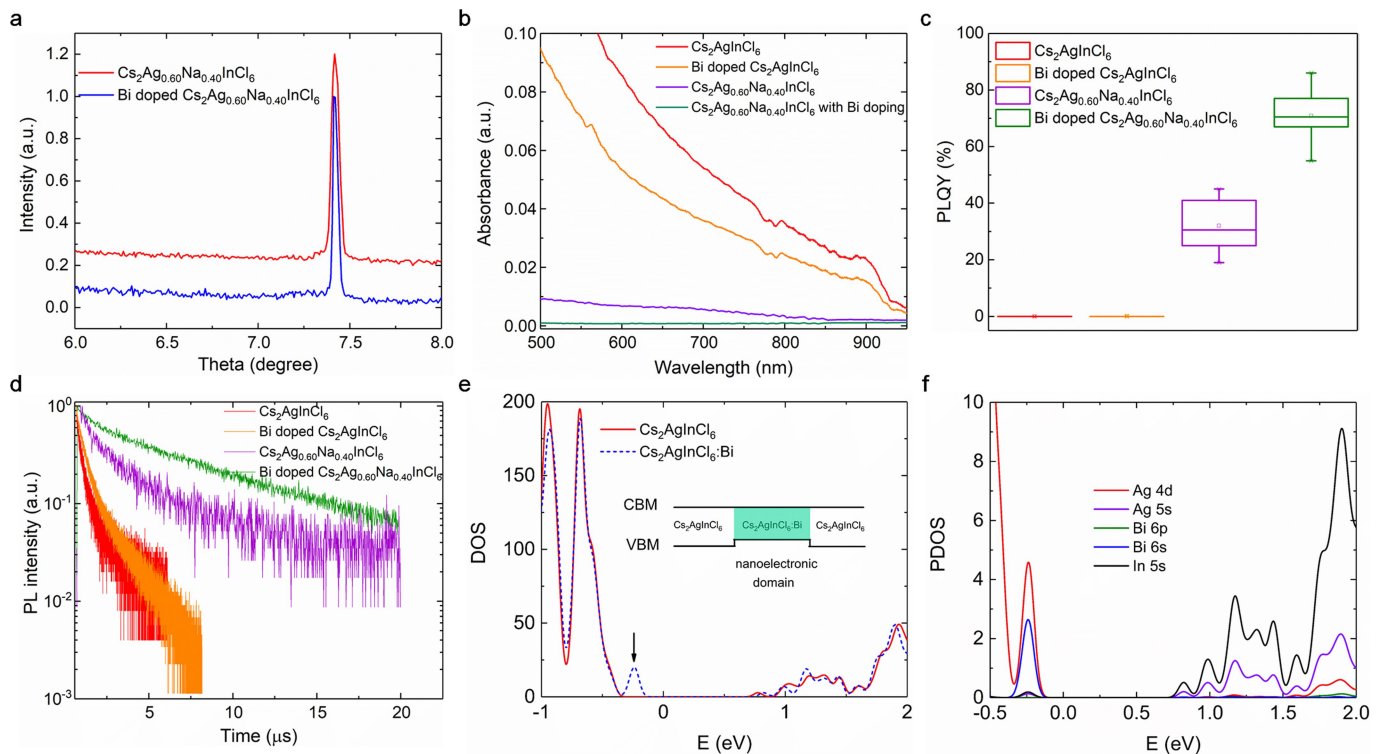


Fig. 3 for details of the characterization). We note that selected-area electron diffraction and scanning electron nanobeam diffraction analysis results (Supplementary Figs. 4, 5) suggest the existence of a microscopic super-lattice (Na/Ag ordering).



**Extended Data Fig. 5 | Photoluminescence enhancement of doped double-perovskite powders. a,** Photoluminescence spectra of pure  $\text{Cs}_2\text{AgInCl}_6$  and Li-doped  $\text{Cs}_2\text{AgInCl}_6$ . **b,** Photoluminescence spectra of pure  $\text{Cs}_2\text{AgSbCl}_6$  and Na-doped  $\text{Cs}_2\text{AgSbCl}_6$ .



**Extended Data Fig. 6 | Characterization of the effect of Bi doping on  $\text{Cs}_2\text{Ag}_x\text{Na}_{1-x}\text{InCl}_6$ .** **a**, High-resolution single-crystal XRD of the (111) peaks of  $\text{Cs}_2\text{Ag}_{0.60}\text{Na}_{0.40}\text{InCl}_6$  with and without Bi doping. **b**, Absorption spectra of various materials with and without Bi doping for wavelengths of 500–950 nm. **c**, PLQY results. **d**, Photoluminescence lifetime. **e**, Comparison of the total density of states (DOS) between pure and

Bi-doped  $\text{Cs}_2\text{AgInCl}_6$ . The inset shows the band alignment of pure and Bi-doped  $\text{Cs}_2\text{AgInCl}_6$ . CBM, conduction band minimum; VBM, valence band maximum. The small shallow peak marked by an arrow is derived from the Bi 6s states, which hybridize with the Ag 4d states. **f**, Partial density of states (PDOS) of Bi-doped  $\text{Cs}_2\text{AgInCl}_6$ .

Extended Data Table 1 | Huang–Rhys factors

Compounds	Huang-Rhys factor
<b>CdSe<sup>53</sup></b>	<b>1</b>
<b>ZnSe<sup>54</sup></b>	<b>0.3</b>
<b>CsPbBr<sub>3</sub><sup>55</sup></b>	<b>3.2</b>
<b>Cs<sub>3</sub>Bi<sub>2</sub>I<sub>9</sub><sup>56</sup></b>	<b>79.5</b>
<b>Cs<sub>3</sub>Sb<sub>2</sub>I<sub>9</sub><sup>56</sup></b>	<b>42.7</b>
<b>Rb<sub>3</sub>Sb<sub>2</sub>I<sub>9</sub><sup>56</sup></b>	<b>50.4</b>
<b>NaCl<sup>57,58</sup></b>	<b>42</b>
<b>AgCl:Br<sup>59</sup></b>	<b>22</b>
<b>Cs<sub>2</sub>NaYCl<sub>6</sub><sup>60</sup></b>	<b>7.0</b>
<b>Cs<sub>2</sub>NaInCl<sub>6</sub></b>	<b>80(ES)/188(GS)*</b>
<b>Cs<sub>2</sub>AgInCl<sub>6</sub></b>	<b>38.7</b>
<b>Cs<sub>2</sub>Ag<sub>0.60</sub>Na<sub>0.40</sub>InCl<sub>6</sub></b>	<b>40.9</b>
<b>Cs<sub>2</sub>Ag<sub>0.16</sub>Na<sub>0.84</sub>InCl<sub>6</sub></b>	<b>51.0</b>

The Huang–Rhys factors for CdSe, ZnSe, CsPbBr<sub>3</sub>, NaCl and AgCl:Br are from the literature, Cs<sub>2</sub>NaInCl<sub>6</sub> is a simulation result and the values for the other materials are obtained from the fitting results of the temperature-dependent FWHM of the photoluminescence data at a relatively low-temperature region (Extended Data Fig. 2c and Supplementary Fig. 1).

\*Normally the Huang–Rhys factors of the ground state and the excited state are similar<sup>49</sup>, as it is generally assumed that these states have the same phonon frequency. However, for Cs<sub>2</sub>NaInCl<sub>6</sub> the difference is quite large: 80 at the excited state and 188 at the ground state.